Chapter 4
The Plunging of Hyperpycnal Plumes on Tilted Bed by Three-Dimensional Large-Eddy Simulations

Felipe Nornberg Schuch, Jorge Hugo Silvestrini, Eckart Meiburg, and Sylvain Laizet

Abstract Theoretical and experimental interest in transport and deposition of sediments from rivers to oceans has increased rapidly over the last two decades. The marine ecosystem is strongly affected by mixing at river mouths, with, for instance, anthropogenic actions like pollutant spreading. Particle-laden flows entering a lighter ambient fluid (hyperpycnal flows) can plunge at a sufficient depth, and their deposits might preserve a remarkable record across a variety of climatic and tectonic settings. Numerical simulations play an essential role in this context since they provide information on all flow variables for any point of time and space. This work offers valuable spatio-temporal information generated by turbulence-resolving 3D simulations of poly-disperse hyperpycnal plumes over a tilted bed. The simulations are performed with the high-order flow solver Xcompact3d, which solves the incompressible Navier–Stokes equations on a Cartesian mesh using high-order finite-difference schemes. Five cases are presented, with different values for flow discharge and sediment concentration at the inlet. A detailed comparison with experimental data and analytical models is already available in the literature. The main objective of this work is to present a new dataset that shows the entire three-dimensional spatio-temporal evolution of the plunge phenomenon and all the relevant quantities of interest.

Keywords Turbidity current · Plunging flow · Computational fluid dynamics · Large-eddy simulation · Xcompact3d

F. N. Schuch (✉) · J. H. Silvestrini
School of Technology, Pontifical Catholic University of Rio Grande do Sul, Porto Alegre, Brazil
e-mail: felipe.schuch@edu.pucrs.br

J. H. Silvestrini
e-mail: jorgehs@pucrs.br

E. Meiburg
Department of Mechanical Engineering, University of California Santa Barbara, Santa Barbara, CA, USA
e-mail: meiburg@engineering.ucsb.edu

S. Laizet
Department of Aeronautics, Imperial College London, London SW7 2AZ, UK
e-mail: s.laizet@imperial.ac.uk

H. F. Meier et al. (eds.), *Advances in Turbulence*, ABCM Series on Mechanical Sciences and Engineering, https://doi.org/10.1007/978-3-031-25990-6_4

4.1 Introduction

Hyperpycnal plumes are produced when the density of a fluid entering a quiescent basin is higher than that in the ambient fluid. They are observed in nature when a river transports enough suspended sediment to be denser than the environment where it flows into, such as channels, lakes, reservoirs, or the ocean (Mulder et al. 2003; Lamb and Mohrig 2009). When the inflow momentum decreases, it eventually plunges under the ambient fluid and flows along the bed as an underflow density current, as illustrated in Fig. 1. The inflow can be characterized by its initial depth $\tilde{h}_0$ (where $\tilde{\cdot}$ corresponds to dimensional quantities), volumetric discharge per unit width $\tilde{Q}_0$ and freshwater density plus an excess due to suspended sediments $\tilde{\rho}_w + \Delta\tilde{\rho}$. The plunging of the hyperpycnal flow can be represented by three main regions. The depth-limited plume is a homogeneous flow region that occupies the complete channel depth, and it is dominated by inertial forces. At sufficient depth $\tilde{H}_p$, the flow collapses in the so-called plunge region. Downstream, a turbidity current is formed, dominated by buoyancy forces, and can be characterized by new values of depth $\tilde{H}_d$, discharge $\tilde{Q}_d$, and density $\tilde{\rho}_a + \Delta\tilde{\rho}_d$, due to continuous mixing between ambient fluid and the underflow (García 1996). Many authors express this increase in flow discharge through the incorporation of ambient fluid in the form of the initial mixture coefficient $\gamma = \tilde{Q}_d/\tilde{Q}_0 - 1$.

The understanding of the parameters and mechanisms that govern the flow transition in the plunge zone is relevant in terms of the health of ecosystems in river deltas regions (Horner-Devine et al. 2015), in the management and operation of dam reservoirs (Chamoun et al. 2016) and in the field of geology, since old sand deposits can preserve records of climatic and tectonic environments (Mulder et al. 2003), in addition to becoming important hydrocarbon reservoirs (Meiburg and Kneller 2010).

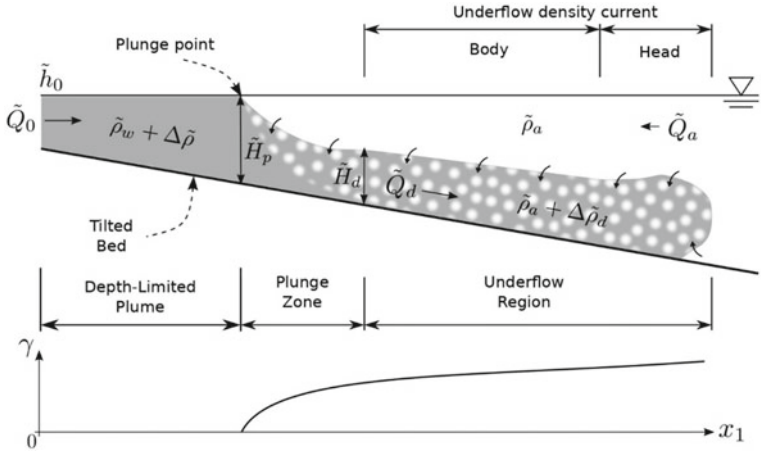

Fig. 1 Illustration of the plunging of an hyperpynal flow in a tilted channel. The mixing coefficient $\gamma = \tilde{Q}_d/\tilde{Q}_0 - 1$ is represented for reference. *Source* Modified from Schuch et al. (2018)

Many studies about this flow configuration are becoming available in the literature, including field observations (Wunderlich and Elder 1973; Ford and Johnson 1981; Best et al. 2005), analytical models (Akiyama and Stefan 1984; Parker and Toniolo 2007; Dai and García 2009), experiments (Singh and Shah 1971; Arita and Nakai 2008; Lamb et al. 2010) and numerical simulations (Farrell and Stefan 1986; Kassem and Imran 2001; Dai et al. 2007). In this context, numerical simulations unlike field observations and experiments can play an important role since they can provide information for all flow variables at any point in time and space. Schuch et al. (2018) presented a new numerical framework for the reproduction and analysis of the plunge phenomenon and its associated flow features, where the results of the three-dimensional turbulence-resolving simulations were compared with experimental data (Lamb et al. 2010) and analytical models (Parker and Toniolo 2007), and good agreement was found between them.

The main objective of this work is to present an original dataset that registers the entire spatio-temporal evolution of the plunge phenomenon and all relevant quantities. To generate this new dataset, the numerical methodology proposed by Schuch et al. (2018) was slightly modified, the simulated time is extended by 20%, the computational domain is six times wider and the flow variables are considered in a layer-averaged context. Additionally, the spatial–temporal data is available online,[1] in order to support future research.

4.2 Methodology

For the present study, N transport equations under the Boussinesq approximation can be used, in addition to the incompressible Navier–Stokes equations. They are written in their dimensionless form as

$$\frac{\partial u_j}{\partial x_j} = 0, \tag{1}$$

$$\frac{\partial u_i}{\partial t} = -u_j \frac{\partial u_i}{\partial x_j} - \frac{\partial p}{\partial x_i} + \frac{1}{\mathrm{Re}} \frac{\partial^2 u_i}{\partial x_j \partial x_j} + e_i^g \frac{1}{\mathrm{Fr}_0^2} \sum_{\updownarrow=1}^{N} c_\updownarrow, \tag{2}$$

$$\frac{\partial c_\updownarrow}{\partial t} = -\left(u_j + u_{s,\updownarrow} e_j^g\right) \frac{\partial c_\updownarrow}{\partial x_j} + \frac{1}{\mathrm{ReSc}} \frac{\partial^2 c_\updownarrow}{\partial x_j \partial x_j}, \updownarrow = 1, \ldots, N, \tag{3}$$

where u_i, p, and c correspond to velocity, pressure, and suspeded particle concentration, respectively, together with the coordinate system x_i (see Fig. 2), time t, unit vector pointing in gravity direction $e^g = [0, 1, 0]$ and the particle's settling velocity u_s. It is related to the particle diameter by the Stokes settling velocity law (Julien

[1] Available at https://doi.org/10.5281/zenodo.3968993 and https://github.com/fschuch/the-plunging-flow-by-3D-LES.

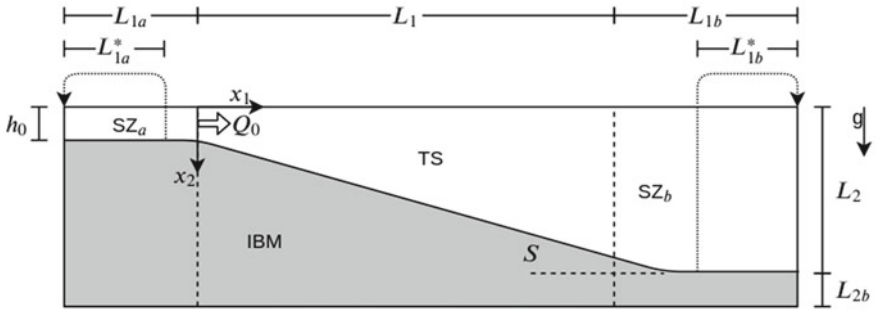

Fig. 2 Schematic representation of the computational domain (not to scale). Spanwise coordinate x_3 is perpendicular to the plane. In gray, the tilted bed is inserted by immersed boundary method (IBM); TS represents the test section, where the flow is analyzed; SZ_a and SZ_b represent the sponge zones. *Source* Modified from Schuch (2020)

1998) which assumes that the dominant flow force on an individual particle is the Stokes drag. The Reynolds, Schmidt, and initial densimetric Froude numbers at the inlet, besides the Stokes settling velocity, are the four dimensionless parameters that describe the problem, they are defined as follows:

$$\mathrm{Re} = \frac{\tilde{Q}_0}{\tilde{\nu}}, \tag{4}$$

$$\mathrm{Sc} = \frac{\tilde{\nu}}{\tilde{D}}, \tag{5}$$

$$\mathrm{Fr}_0 = \frac{\tilde{Q}_0}{\sqrt{R\tilde{C}_0\tilde{g}\tilde{h}^3}}, \tag{6}$$

$$u_{s,\updownarrow} = \frac{\tilde{u}_{s,\updownarrow}\tilde{h}_0}{\tilde{Q}_0} = \frac{\tilde{d}^2_{s,\updownarrow}R\tilde{g}\tilde{h}_0}{18\tilde{\nu}\tilde{Q}_0}, \updownarrow = 1, \ldots, N, \tag{7}$$

where $\tilde{Q}_0$ and $\tilde{C}_0$ are the volumetric discharge per unit width and volumetric sediment concentration at the inlet of the channel, respectively. The kinematic viscosity is $\tilde{\nu}$, the fresh water and sediment densities are $\tilde{\rho}_w$, $\tilde{\rho}_s$, with R defined as $(\tilde{\rho}_s - \tilde{\rho}_w)/\tilde{\rho}_w$. The gravity acceleration is $\tilde{g}$, the diffusivity of particle concentration is $\tilde{D}$ and the grain size is $\tilde{d}_s$. All parameters and variables are made dimensionless using the influx velocity $\tilde{U}_0$, depth $\tilde{h}_0$ and sediment concentration $\tilde{C}_0$.

The computational setup (see Fig. 2) is based on the experimental channel configuration of Lamb et al. (2010) and the numerical study of Schuch et al. (2018). The test section (TS) is the region where the flow is analyzed, whose dimensions are $(L_1, L_2, L_3) = (250.0h_0, 16.875h_0, 24.0h_0)$. Notice that the dimensionless initial

depth is $h_0 = 1$. The bed slope $S = 5\%$ is included in the computational domain via an immersed boundary method (IBM), following the alternating direction forcing strategy proposed by Gautier et al. (2014). Two sponge zones are employed for different reasons. Firstly, SZ_a provides the particle-laden flow upstream of the test section, with a recycling technique in order to generate a turbulent inflow condition. Secondly, SZ_b applies an intrinsic profile for the stream-wise velocity u_1 near the outflow boundary, in order to reduce the turbulence level to zero. The horizontal extension of the sponge zones is $(L_{1a}, L_{1b}) = (25.0, 62.5)$. The entire computational domain is discretized using $(n_1, n_2, n_3) = (1081, 121, 90)$ mesh points. A time step of $\Delta t = 0.0125$ is employed for a total of 4.8×10^5 iterations. In comparison with the previous study of Schuch et al. (2018), the numerical channel in this study is now six times wider, in a dimension compatible with the experimental reference if an initial depth of $\tilde{h}_0 = 10$ mm is considered, and the simulated time is extended from 5,000 to 6,000 dimensionless units, an increase of 20%. A nondeformable water surface is imposed as top boundary condition (where $x_2 = 0$), which is described by Nasr-Azadani et al. (2013) as a free-slip condition for velocity and no-flux condition for the concentration field. The bottom boundary condition (at the solid/fluid interface) is no-slip for velocity and one-dimensional convective outflow for concentration, as functions of the settling velocity u_s (Necker et al. 2002). Inflow and outflow conditions are handled by both sponges zones and periodic boundary condition is employed in the spanwise direction (x_3). For the initial condition, the domain is filled with freshwater at rest ($u_i = c_{\updownarrow} = 0$). For more details about the computational setup see Schuch (2020).

The numerical simulations were carried out by the high-order Navier–Stokes solver Xcompact3d,[2] an open-source tool based on the Boussinesq system for incompressible fluids, designed for High-Performance Computing (Laizet and Lamballais 2009; Laizet and Li 2011; Bartholomew et al. 2020). The governing equations (2) are solved under an implicit Large-Eddy Simulations approach, in which only the largest and energy-containing flow structures are resolved. On the other hand, the small scales are not resolved, instead, they are modeled via an artificial dissipation that takes place when computing the viscous term (Sagaut 2006; Grinstein et al. 2007; Lamballais et al. 2011; Dairay et al. 2017).

Seven experiments were carried out by Lamb et al. (2010), and five of them are reproduced in this study, as shown in Table 1. The experimental grain-size distribution (crushed silica $\tilde{\rho}_s = 2{,}650\,\text{kg/m}^3$) is modeled by three diameters ($\tilde{d}_{s,1} = 3\,\mu\text{m}$, $\tilde{d}_{s,2} = 21\,\mu\text{m}$, and $\tilde{d}_{s,3} = 43\,\mu\text{m}$) in a distribution of about one third for each grain size. The Schmidt number Sc is equal to 1 in the present study. Notice that cases 2, 6, and 7 have the same flow discharge $\tilde{Q}_0$ and increasing sediment concentration $\tilde{C}_0$, while cases 4, 5, and 6 have the same sediment concentration $\tilde{C}_0$ and increasing flow discharge $\tilde{Q}_0$. The validation of the numerical framework employed here for the problem illustrated in Fig. 1 is out of the scope of this study, since a complete comparison between numerical, experimental, and analytical models is already available in Schuch et al. (2018).

[2] The code is available at https://github.com/xcompact3d/Incompact3d.

Table 1 Volumetric discharge per unit width $\tilde{Q}_0$ and volumetric sediment concentration $\tilde{C}_0$ recorded at the inlet from the experiments of Lamb et al. (2010), in addition to the respective Reynolds number Re, initial densimetric Froude number Fr_0 and Stokes settling velocity $u_{s,\updownarrow}$ for each granulometric fraction

Simulations	2	4	5	6	7
$\tilde{Q}_0$ (m^2/s)	0.0043	0.0025	0.0033	0.0043	0.0043
$\tilde{C}_0$ (%)	0.36	0.54	0.54	0.54	1.00
Re	4,300	2,500	3,300	4,300	4,300
Fr_0	17.81	8.45	11.16	14.54	10.68
$u_{s,1} \times 10^{-5}$	1.9	3.2	2.5	1.9	1.9
$u_{s,2} \times 10^{-3}$	0.9	1.6	1.2	0.9	0.9
$u_{s,3} \times 10^{-3}$	3.9	6.7	5.0	3.9	3.9

Source Modified from Lamb et al. (2010)

4.3 Results

A sample of the tridimensional plunging flow is shown in Fig. 3, represented by a snapshot of the total concentration field ($c_t = c_1 + c_2 + c_3$) for case 4 at dimensionless time equals to $t = 1{,}000$. In this figure, the plunge line is visible near $x_1 = 120$, as well as the body and head of the underflow turbidity current downstream plunging, including the lobes and clefts structures at the front. The dimensionless total concentration is one (red color) right at the inlet of the test section, and then decays due to sedimentation with the stream-wise coordinate x_1. Besides that, the turbulent mixing between the turbidity current and the ambient fluid is evidenced by the dark blue color, which corresponds to low concentration levels.

The complete spatio-temporal analysis of the relevant quantities is possible in a layer-averaged context per width unit, that is computed following Ellison and Turner (1959) according to the equations:

$$Uh(x_1, t) = \frac{1}{L_3} \int_0^{L_3} \int_{x_{2r}}^{x_{2i}} u_1(x_1, x_2, x_3, t) dx_2 dx_3, \tag{8}$$

$$U^2 h(x_1, t) = \frac{1}{L_3} \int_0^{L_3} \int_{x_{2r}}^{x_{2i}} (u_1(x_1, x_2, x_3, t))^2 dx_2 dx_3, \tag{9}$$

$$UCh(x_1, t) = \frac{1}{L_3} \int_0^{L_3} \int_{x_{2r}}^{x_{2i}} u_1(x_1, x_2, x_3, t) c_t(x_1, x_2, x_3, t) dx_2 dx_3. \tag{10}$$

For the vertical integration, x_{2r} represents the bed position and x_{2i} represents the interface between the underflow turbidity current and the ambient fluid, considered in this work as the position where $u_1 \times c_t = 0.005$. Finally, the layer-averaged velocity U, flow depth H, flow discharge Q, concentration C, and local densimetric Froude number Fr are obtained, respectively, as

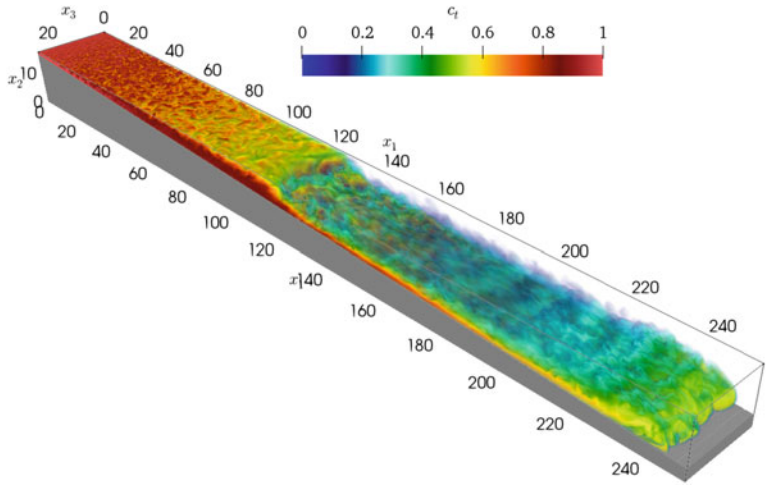

Fig. 3 Instantaneous volumetric visualization of the total concentration field c_t for case 4 at $t = 1{,}000$

$$U(x_1, t) = U^2 h / Uh, \tag{11}$$

$$H(x_1, t) = (Uh)^2 / U^2 h, \tag{12}$$

$$Q(x_1, t) = Uh, \tag{13}$$

$$C(x_1, t) = UCh / Uh, \tag{14}$$

$$\mathrm{Fr}(x_1, t) = \frac{Q(x_1, t)}{\sqrt{C(x_1, t)(H(x_1, t))^3}} \mathrm{Fr}_0. \tag{15}$$

The spatio-temporal evolution of the quantities described above for case 4 are shown in Fig. 4, in addition to the spanwise-averaged total concentration field c_t for dimensionless time equals to 250, 500, 1,000, 2,000, and 6,000, from (a) to (e), respectively. All the features of the plunging flow in a tilted bed (see Fig. 1) can be seen. The plunge point is visible since early times (a and b) and moves downstream, for more advanced time (e) it tends to a quasi-stationary position at around $x_1 = 150$, the same position found experimentally in Lamb et al. (2010). Upstream plunging is located at the depth-limited flow region, where the inflowing turbidity current has enough momentum to push the ambient fluid downstream. Due to the tilted bed, the flow's depth increases with the streamwise coordinate (x_1) and progressively reduces its velocity until a critical point, the plunge zone, where the flow collapses, accelerates, and turns into a density current, governed now by the buoyance forces. This behavior reflects on the layer-averaged velocity U (f), where the maximum

value is noticeable at the inflow boundary ($x_1 = 0$) and decreases until its minimum value at the plunge point, where the flow accelerates. Besides that, the incorporation of ambient fluid into the submerged turbidity current (entrainment) increases the flow velocity downstream plunging. The layer-averaged concentration C (g) decays with x_1 due to the sedimentation, and the mixing with the ambient fluid reduces concentration even more downstream plunging. Besides that, C works as an indicator for the temporal evolution of the front position x_f, which is obtained as the highest value of x_1 where the concentration is non-zero. The densimetric Froude number Fr (h) expresses the ratio between inertial and buoyance forces, that are dominant upstream and downstream plunging, respectively. In this way, Fr is directly related to the stable plunge position, in fact, the Froude value at plunge point observed in Fig. 4h is very close to $\mathrm{Fr}_p = 0.45$, a value reported in previous works (Parker and Toniolo 2007; Lamb et al. 2010; Schuch et al. 2018). The densimetric Froude number is also used to track the temporal evolution of the plunge point position x_p, since it is observed at the absolute minimum value for Fr.

If the flow is sufficiently intense, the turbidity currents can resuspend part of the material previously deposited, or even erode the bed over which it flows, as commented by Necker et al. (2002). Even though the numerical configuration of this work does not consider resuspension, a further analysis based on the simulated data can indicate places where the flow is more likely to present such phenomena. For that, the bed shear velocity u_τ has a fundamental role, and can be calculated according to the equation:

$$u_\tau = \sqrt{\tau_w}, \text{with} \tau_w = \frac{1}{\mathrm{Re}} \sqrt{\left(\frac{\partial \hat{u}_1}{\partial \hat{x}_2}\right)^2 + \left(\frac{\partial \hat{u}_3}{\partial \hat{x}_2}\right)^2} \Bigg|_{x_2 = x_{2i}}. \tag{16}$$

The notation $\hat{(\cdot)}$ represents a rotation in the coordinate system, so that $\hat{x}_1$ still points in the preferred flow direction, but is now parallel to the bed, and $\hat{x}_2$ is normal to the bed, while x_{2i} corresponds to the position of the solid–fluid interface. In this way, the velocities required for the calculation are given by

$$\hat{u}_1 = \cos(\theta) u_1 - \sin(\theta) u_2, \tag{17}$$

$$\hat{u}_3 = u_3, \tag{18}$$

while the derivative normal to the bed is computed as

$$\frac{\partial}{\partial \hat{x}_2} = \sin(\theta) \frac{\partial}{\partial x_1} + \cos(\theta) \frac{\partial}{\partial x_2}. \tag{19}$$

The bed shear velocity u_τ can be observed in Fig. 4i. It has a behavior very similar to that observed for the layer-averaged velocity U, being maximum at the entrance of the channel and then decreases. The minimum value for u_τ is reached exactly

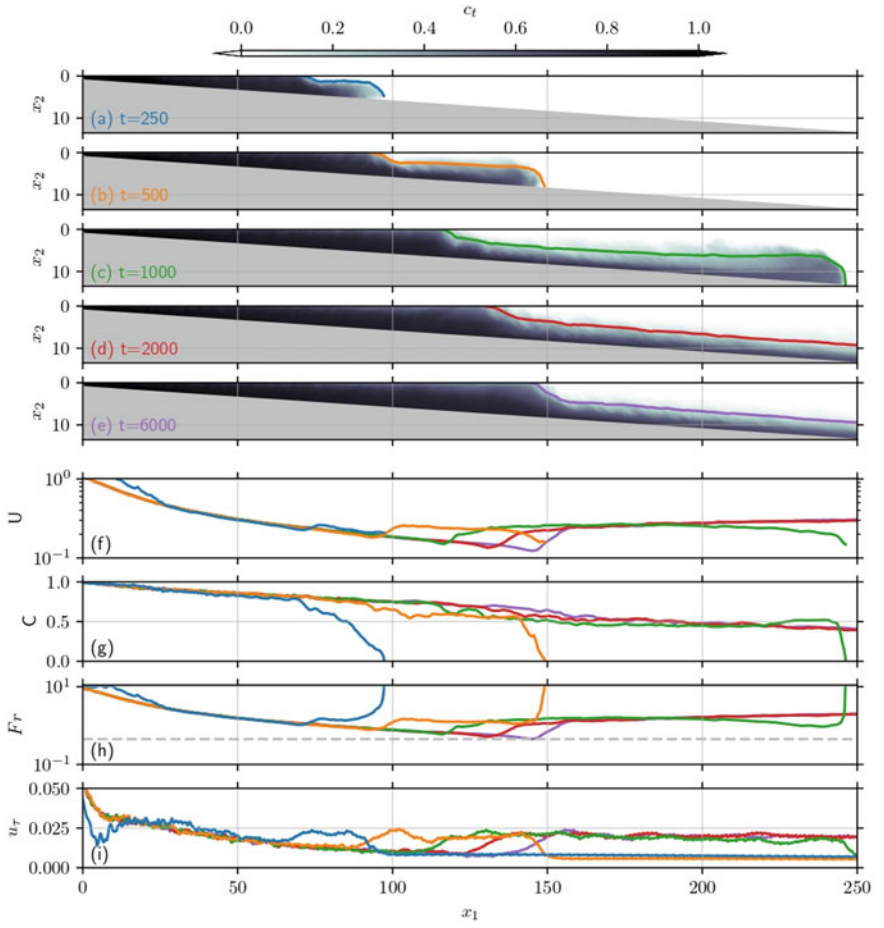

Fig. 4 Case 4 spanwise-averaged total concentration field c_t for dimensionless time equals to 250, 500, 1,000, 2,000, and 6,000 from (**a**) to (**e**), respectively. In addition to layer-averaged flow depth H (colored lines from **a** to **e**), streamwise velocity U (**f**), concentration C (**g**), and local densimetric Froude number Fr (**h**), $\mathrm{Fr}_p = 0.45$ is shown in dashed line for reference, computed according to Eq. (4), besides the spanwise-averaged bed shear velocity u_τ (**i**), expressed by Eq. (16)

where the reduction in flow's depth occurs, seen solid lines from (a) to (e), there is a local maximum immediately at the plunge point, where Fr is minimum, and then the value stabilizes in the body region, being slightly larger at the head. It indicates that the channel's entrance is the region with the greatest erosive potential, followed by the plunging point and then the head of the turbidity current.

The spanwise-averaged total concentration field c_t for all cases at dimensionless time $t = 1{,}000$ is shown in Fig. 5, from (a) to (e). Both flow head and plunging zone are well defined for all cases, however, their position is affected by the parameters of each case. In comparison, a plunging upstream accelerates the turbidity current

earlier and impulsionates its body and head, as shown in the layer-averaged velocity U (f). The layer-averaged concentration C (g) is very similar for all cases upstream plunging, however, the value downstream differs due to differences in flow depth and mixing with the ambient fluid. The densimetric Froude number Fr is shown in Fig. 5h. At $t = 1{,}000$, the plunging for all cases is still in the transient phase, so the Froude value observed at plunge point is higher than the reference of $\mathrm{Fr}_p = 0.45$, on the other hand, the Fr value measured at underflow's head of around a unity is in agreement with previous studies (Sequeiros 2012; Sequeiros et al. 2018). Figure 5i shows the bed shear velocity for the different cases. In general, the maximum value for u_τ is where $x_1 = 0$, followed by underflow's head and body, and the minimum value is observed at the plunge point. The magnitude of u_τ is function of the flow velocity, that in turn depends on the plunge point location, therefore, cases with the plunging upstream produce higher bed shear velocity u_τ. The animated versions of the flow visualization are presented in Figs. 3, 4, and 5 are available as supplementary materials.

Figure 6a shows the temporal evolution of the plunge point position x_p. Cases 2, 6, and 7 have the same flow discharge and increasing sediment concentration, which moves the plunge point downstream. Additionally, cases 4, 5, and 6 have the same sediment concentration and increasing flow discharge, which also moves the plunge downstream. Both parameters can be combined into the initial densimetric Froude number Fr_0, where a higher Fr_0 demands more distance for plunging and more runtime to eventually reach an asymptotic state. It is evident that for case 2, with the highest initial Froude number, the plunge zone left the computational test section at around $t = 4{,}000$. Notice that the depth at plunge point is recovered by the linear equation $h_p = 1 + Sx_p$. Figure 6b shows the temporal evolution of the front position x_f, while Fig. 6c shows the front velocity $u_f = dx_f/dt$, where a moving average in time is employed in order to smooth the signal. Notice that both curves are just defined while the front is inside the test section ($x_f \leq 250$). As discussed previously, the front velocity is strongly affected by the plunge point position, once it impulsions the underflow's body and head. In this way, a higher front velocity is observed according to the same parameters that move the plunge point upstream, i.e., lower initial densimetric Froude number Fr_0, lower initial flow discharge Q_0 or higher initial sediment concentration C_0. Finally, Fig. 6d shows the time evolution of the densimetric Froude number at plunge position Fr_p, where a convergence to $\mathrm{Fr}_p = 0.45$ is noticeable, in good agreement with previous studies (Parker and Toniolo 2007; Lamb et al. 2010; Schuch et al. 2018). The averaged Froude number at plunge point measured is $\mathrm{Fr}_p = 0.438 \pm 0.027$, taking an average in time ($4{,}000 \leq t \leq 6{,}000$) and between cases (excluding case 2, that left the computational test section). This value depends on the bed roughness, suspended grain size, and bed slope, according to Sequeiros (2012). Besides, Fr_p can be useful in the development of new methodologies for the prediction of depth for plunging, or plunging criteria (Schuch 2020; Schuch et al. 2021).

Figure 7 shows the flow quantities under investigation as a function of time t and the streamwise coordinate x_1, are they: Flow depth H, layer-averaged concentration C and densimetric Froude number Fr, computed according to Eq. (4), in

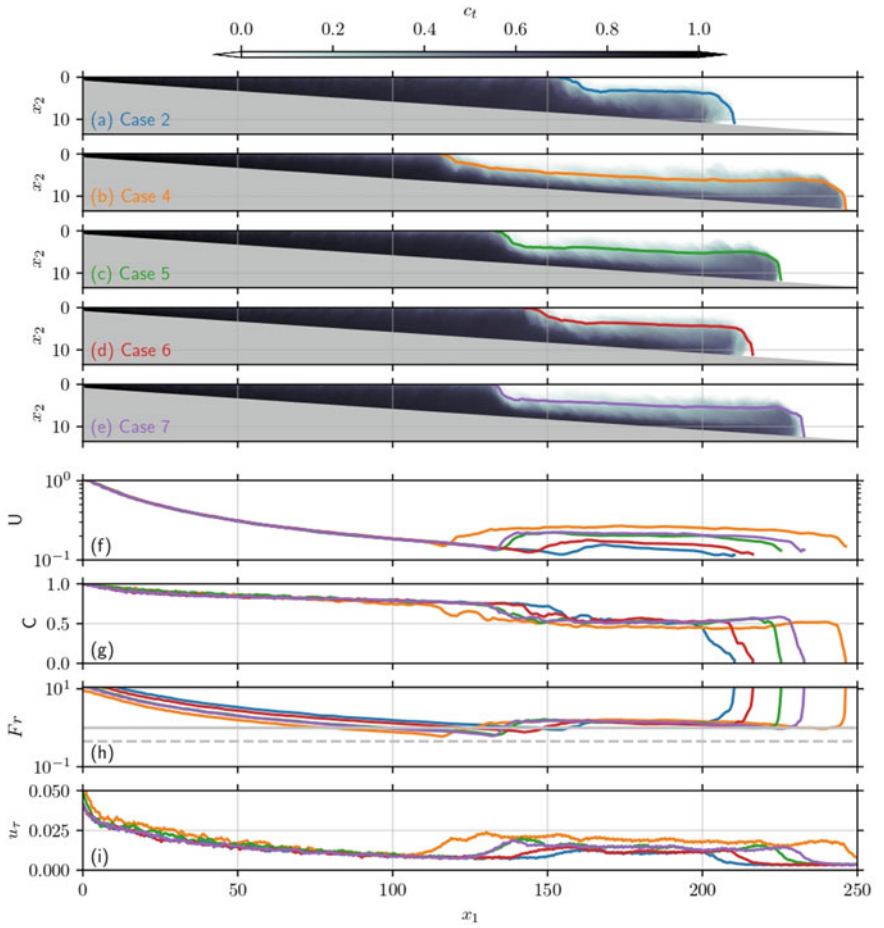

Fig. 5 Spanwise-averaged total concentration field c_t for all cases from (**a**) to (**e**) at $t = 1{,}000$. In addition to layer-averaged flow depth H (colored lines from **a** to **e**), streamwise velocity U (**f**), concentration C (**g**), and local densimetric Froude number Fr (**h**), 1.0 and 0.45 are shown in solid and dashed lines for reference, computed according to Eq. (4), besides the spanwise-averaged bed shear velocity u_τ (**i**), expressed by Eq. (16)

addition to the mixing coefficient $\gamma = Q/Q_0 - 1$ and the bed shear velocity u_τ (16), from top to bottom, respectively. The positions for plunge point x_p (solid lines) and front x_f (dashed lines) are presented for reference. The five simulated cases are arranged horizontally. The entire spatio-temporal evolution is shown, where some topics discussed previously in Figs. 4 and 5 are visible in details. The maximum flow depth H (Fig. 7a–e) occurs at plunge point, where the flow collapses and accelerates. The plunge point for case 2 left the test section (where $x_1 = 250$), its high initial Froude number demands a deeper domain in order to have a stable plunging position. The concentration C (Fig. 7f–j) decays due to sedimentation, and the mixing with the

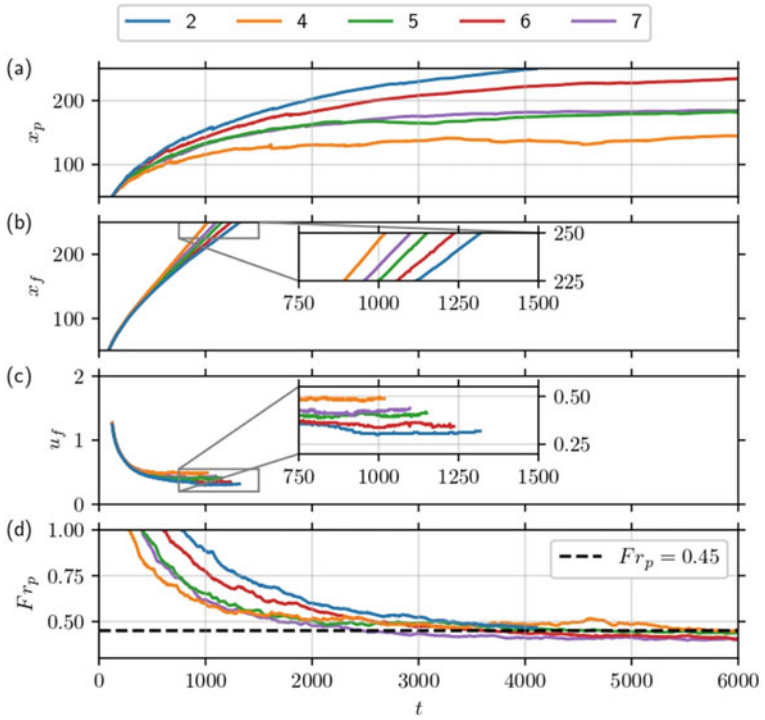

Fig. 6 Time evolution of **a** distance for plunging x_p, **b** front position x_f, **c** front velocity u_f and **d** densimetric Froude number at plunging point Fr_p, where $\mathrm{Fr}_p = 0.45$ is shown for reference

ambient fluid downstream plunging is another process that reduces sediment concentration. The densimetric Froude number Fr (Fig. 7f–j) decreases with the streamwise coordinate x_1, because the flow depth increases, until the minimum value at plunge zone. The acceleration at plunge zone increases Fr downstream plunging, as well as the increase in flow discharge due to entrainment. The densimetric Froude number measured downstream plunging Fr_d (at the end of the test section, where $x_1 = 250$) is equal to 1.93 ± 0.043, 1.722 ± 0.044, 1.385 ± 0.113 and 1.648 ± 0.047 for cases 4 to 7, respectively, all greater than one (e.g., supercritical), which is expected once the head has passed away in bed slopes steeper than about 1% according to Sequeiros (2012). Figure 7p–t show the spanwise-averaged bed shear velocity u_τ, the highest value is observed for case 4 (Fig. 7q), with the shortest distance for plunging and higher underflow velocity. Figure 7u–y shows the mixing coefficient $\gamma = Q/Q_0 - 1$, that represents the increase in the submerged flow discharge due to entrainment of ambient fluid into the turbidity current. Cases that have plunged early present more distance for entrainment, so the highest value is observed for case 4 (Fig. 7v), followed by case 7 (Fig. 7y) and case 5 (Fig. 7w). The plunging point for case 2 (Fig. 7u) left the computational test section, so the mixing coefficient is negligible for $t > 4{,}000$. On the other hand, this case has a negative mixing value

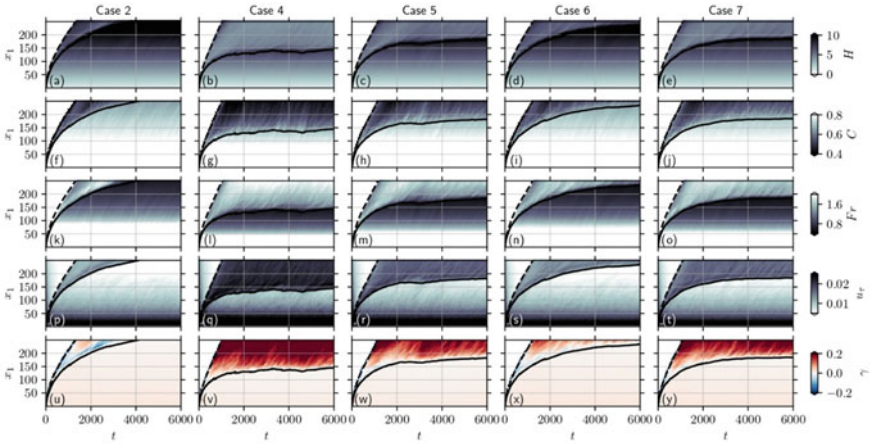

Fig. 7 Spatio-temporal evolution of flow depth H, layer-averaged concentration C, densimetric Froude number Fr, spanwise-averaged bed shear velocity u_τ and mixing coefficient, from top to bottom, respectively. Cases 2, 4, 5, 6, and 7 are arranged from left to right. Plunging point x_p (solid lines) and front x_f (dashed lines) positions are shown for reference. Horizontal and vertical axes represent time t and stream-wise coordinate x_1, respectively

(blue color) downstream plunging during the transient phase ($t < 4{,}000$), indicating that the submerged turbidity current loses its volume to the ambient in a detrainment process. Notice that a pulsing phenomenon is observed for all cases, even though the variables are evaluated in a spanwise-averaged context and the input flow is kept steady, this phenomenon is investigated in details in Best et al. (2005) and Kostaschuk et al. (2018).

4.4 Conclusions

Numerical simulations play an essential role in many different research fields, since they can provide information on all variables for any point of time and space. Lab experiments are very often not able to provide such information, with data only available in a plane and/or locally. In this study, a new dataset is presented, covering the entire spatio-temporal evolution of the plunge phenomenon and all quantities related to it using the layer-averaged context. Such database can be used to analyze the parameters and mechanisms that govern the flow transition in the plunge zone and support future research, it is available at https://doi.org/10.5281/zenodo.3968993 and https://github.com/fschuch/the-plunging-flow-by-3D-LES.

Acknowledgements This study was supported by Petrobras S.A. and financed in part by the Coordenação de Aperfeiçoamento de Pessoal de Nível Superior—Brazil (CAPES)—Finance Codes

88887.154060/2017-00 and 88881.187490/2018-01. Computing time was provided by the high-performance facility LAD-PUCRS at the Pontifical Catholic University of Rio Grande do Sul, in Porto Alegre, Brazil.

References

Akiyama J, Stefan HG (1984) Plunging flow into a reservoir: theory. J Hydraul Eng 110(4):484–499. ISSN 0733-9429. https://doi.org/10.1061/(ASCE)0733-9429(1984)110:4(484)

Arita M, Nakai M (2008) Plunging conditions of two-dimensional negative buoyant surface jets released on a sloping bottom. J Hydraul Res 46(3):301–306

Bartholomew P, Deskos G, Frantz RA, Schuch FN, Lamballais E, Laizet S (2020) Xcompact3d: an open-source framework for solving turbulence problems on a Cartesian mesh. SoftwareX 12:100550

Best JL, Kostaschuk RA, Peakall J, Villard PV, Franklin M (2005) Whole flow field dynamics and velocity pulsing within natural sediment-laden underflows. Geology 33(10):765–768

Chamoun S, De Cesare G, Schleiss AJ (2016) Managing reservoir sedimentation by venting turbidity currents: a review. Int J Sedim Res 31(3):195–204

Dai A, Cantero MI, García MH (2007) Plunging of two-dimensional gravity currents. In: Proceedings of the 5th international symposium on environmental hydraulics, IAHR, Temp, Ariz

Dai A, García MH (2009) Discussion of "note on the analysis of plunging of density flows" by Gary Parker and Horacio Toniolo. J Hydraul Eng 135(6):532–533

Dairay T, Lamballais E, Laizet S, Vassilicos JC (2017) Numerical dissipation vs. subgrid-scale modelling for large eddy simulation. J Comput Phys 337:252–274

Ellison T, Turner J (1959) Turbulent entrainment in stratified flows. J Fluid Mech 6(3):423–448

Farrell G, Stefan H (1986) Buoyancy induced plunging flow into reservoirs and coastal regions, project report, no. 241, st. Anthony Falls Hydr. Lab., University of Minnesota

Ford DE, Johnson MC (1981) Field observations of density currents in impoundments. In: Surface water impoundments. ASCE, pp 1239–1248

García M (1996) Hidrodinamica ambiental. Colección Ciencia y técnica, Universidad Nacional del Litoral

Gautier R, Laizet S, Lamballais E (2014) A DNS study of jet control with microjets using an immersed boundary method. Int J Comput Fluid Dyn 28(6–10):393–410

Grinstein FF, Margolin LG, Rider WJ (2007) Implicit large eddy simulation: computing turbulent fluid dynamics. Cambridge University Press

Horner-Devine AR, Hetland RD, MacDonald DG (2015) Mixing and transport in coastal river plumes. Annu Rev Fluid Mech 569–594

Julien PY (1998) Erosion and sedimentation. Cambridge University Press, Cambrige, Reino Unido

Kassem A, Imran J (2001) Simulation of turbid underflows generated by the plunging of a river. Geology 29(7):655–658

Kostaschuk R, Nasr-Azadani MM, Meiburg E, Wei T, Chen Z, Negretti ME, Best J, Peakall J, Parsons DR (2018) On the causes of pulsing in continuous turbidity currents. J Geophys Res Earth Surf 123(11):2827–2843

Laizet S, Lamballais E (2009) High-order compact schemes for incompressible flows: a simple and efficient method with quasi-spectral accuracy. J Comput Phys 228(16):5989–6015

Laizet S, Li N (2011) Incompact3d: a powerful tool to tackle turbulence problems with up to $O(105)$ computational cores. Int J Numer Methods Fluids 67(11):1735–1757

Lamb MP, McElroy B, Kopriva B, Shaw J, Mohrig D (2010) Linking river-flood dynamics to hyperpycnalplume deposits: experiments, theory, and geological implications. Geol Soc Am Bull 122(9–10):1389–1400

Lamb MP, Mohrig D (2009) Do hyperpycnal-flow deposits record river-flood dynamics? Geology 37(12):1067–1070

Lamballais E, Fortuné V, Laizet S (2011) Straightforward high-order numerical dissipation via the viscous term for direct and large eddy simulation. J Comput Phys 230(9):3270–3275

Meiburg E, Kneller B (2010) Turbidity currents and their deposits. Annu Rev Fluid Mech 42:135–156

Mulder T, Syvitski JPM, Migeon S, Faugeres JC, Savoye B (2003) Marine hyperpycnal flows: initiation, behavior and related deposits. A review. Mar Pet Geol 20(6):861–882

Nasr-Azadani M, Hall B, Meiburg E (2013) Polydisperse turbidity currents propagating over complex topography: comparison of experimental and depth-resolved simulation results. Comput Geosci 53:141–153

Necker F, Härtel C, Kleiser L, Meiburg E (2002) High-resolution simulations of particle-driven gravity currents. Int J Multiph Flow 28(2):279–300

Parker G, Toniolo H (2007) Note on the analysis of plunging of density flows. J Hydraul Eng

Sagaut P (2006) Large eddy simulation for incompressible flows: an introduction. Springer Science & Business Media

Schuch FN, Meiburg E, Silvestrini JH (2021) Plunging condition for particle-laden flows over sloping bottoms: three-dimensional turbulence-resolving simulations. Comput Geosci 156(2021):104880

Schuch FN, Pinto LC, Silvestrini JH, Laizet S (2018) Three-dimensional turbulence-resolving simulations of the plunge phenomenon in a tilted channel. J Geophys Res: Oceans 123:1–13

Schuch FN (2020) Análise do Mergulho de Escoamentos Hiperpicnais em Canal Inclinado por Meio de Simulação Numérica de Grandes Escalas. Ph.D. thesis, Programa de Pós-Graduação em Engenharia e Tecnologia de Materiais, Escola Politécnica, PUCRS

Sequeiros OE (2012) Estimating turbidity current conditions from channel morphology: a froude number approach. J Geophys Res: Oceans 117(C4)

Sequeiros OE, Mosquera R, Pedocchi F (2018) Internal structure of a self-accelerating turbidity current. J Geophys Res: Oceans 123(9):6260–6276

Singh B, Shah C (1971) Plunging phenomenon of density currents in reservoirs. La Houille Blanche 1:59–64

Wunderlich WO, Elder RA (1973) Mechanics of flow through man-made lakes. In: Washington DC American Geophysical Union Geophysical Monograph Series, vol 17, pp 300–310